ISSN 1573-160X, *PHYSICAL OCEANOGRAPHY*, Vol. 32, Iss. 4, pp. 537-557 (2025)
Original Russian Text © A. A. Pavlushin, 2025,
published in *Morskoy Gidrofizicheskiy Zhurnal*, 2025, Vol. 41, Iss. 4, pp. 515–536

Original article

Numerical Simulation of Deep Currents in the Black Sea Using a Two-Layer Eddy-Resolving Model

A. A. Pavlushin

Marine Hydrophysical Institute of RAS, *Sevastopol*, *Russian Federation*
✉ *pavlushin@mhi-ras.ru*

Abstract
Purpose. The purpose of this study is to calculate and construct maps of deep currents in the Black Sea and to identify the key characteristics of deep-sea circulation.
Methods and Results. A two-layer eddy-resolving model incorporating actual bathymetry was used to simulate the currents. The motion was driven by wind shear stress with mean annual cyclonic vorticity. Long-term simulations yielded fields of current velocity and layer thickness for both upper and lower layers. The kinetic energy of mean and "eddy" currents was calculated and the parameters of wave oscillations in the current velocity field were determined.
Conclusions. The simulation results revealed a closed current system transporting water in a cyclonic direction in the deep layer of the Black Sea, driven by wind with cyclonic vorticity. The primary features of deep-sea circulation are eddies distributed across the continental slope and continental rise. The Rim Current instability, along with topographic and planetary β-effects, contributes possibly to the formation of eddy structures in the deep Black Sea.

Keywords: Black Sea, large-scale circulation, deep currents, mathematical modeling, topographic β-effect, planetary β-effect, Rossby waves

Acknowledgments: T he study was carried out within the framework of state assignment of FSBSI FRC MHI on themes FNNN-2023-0003 and FNNN-2024-0012.

For citation: Pavlushin, A.A., 2025. Numerical Simulation of Deep Currents in the Black Sea Using a Two-Layer Eddy-Resolving Model. *Physical Oceanography*, 32(4), pp. 537-557.

Introduction

The large-scale water circulation in the Black Sea is considered well-studied by the scientific community. Instrumental observations of currents span over a century. The circulation scheme, with the meandering Rim Current (RC) as its primary component encircling the deep-water part of the sea, was first described by Soviet scientist N. M. Knipovich in 1932 [1]. He proposed the existence of two separate large-scale cyclonic eddies within the RC, giving rise to the term "Knipovich's glasses." Since then, this circulation scheme has undergone only minor refinements [1].

In addition to the RC, the large-scale circulation in the Black Sea includes eddy formations, primarily anticyclones, forming in the meander troughs between the RC

[1] Knipovich, N.M., 1932. The Hydrological Investigations in the Black Sea Area. *Trudy Azovo-Chernomorskoy Nauchnopromyslovoy Ekspeditsii*, 10(10), p. 274 p. (in Russian).

and the coast. Typically, their spatial scale ranges from 30 to 150 km. In scientific literature these eddies are referred to as mesoscale vortices while the RC is classified as a large-scale current. However, according to A. S. Monin's classification [2], mesoscale vortices correspond to synoptic variability processes whereas the RC corresponds to seasonal variability. The most frequently observed anticyclonic vortices to the right of the RC are the quasi-stationary Batumi anticyclone located near the eastern coast and the Sevastopol anticyclone west of the Crimean Peninsula [1].

It is important to note that all the aforementioned elements of large-scale circulation exist only in the water layer above the main pycnocline [2]. The movement of water masses below the pycnocline to the seabed, which constitutes deep-water circulation, remains poorly understood despite long-term observations as direct measurements of currents at great depths over extended periods are labor-intensive and costly.

The lack of sufficient observational data has led to diverse and often conflicting hypotheses about the strength and direction of deep currents. Some hypotheses suggest the absence of such currents while others propose variable-direction currents. Notably, sporadic measurements of current parameters at great depths have been conducted. Results from analyzing multiyear observational data in the Oceanographic Data Bank (ODB) of Marine Hydrophysical Institute, reported in [3], indicate that variable-direction currents with velocities up to 25 cm/s can exist in the deep Black Sea.

In the 21st century, new methods have emerged for studying deep-sea currents in the Black Sea. First, Argo floats, deployed in the Black Sea since 1999, have been used to collect data. Although they do not directly measure current parameters, these floats enable the calculation of trajectories and mean velocities based on displacement at specific depths.

Analysis of a large dataset from Argo floats [4] revealed that deep-sea currents moved cyclonically along isobaths at mean velocities of 4–6 cm/s. Given the thickness of the water layer below the pycnocline, the mass of water transported by these currents exceeds that carried by the RC. This indicates that deep-sea currents are significant and not negligible.

In 2016, scientists from Shirshov Institute of Oceanology of RAS and Marine Hydrophysical Institute of RAS deployed a moored buoy station on the Black Sea continental slope. For one year, current parameters were measured at a depth of 1700 m using an Acoustic Doppler Current Profiler (ADCP) [5]. These measurements revealed horizontal velocity oscillations of ±15 cm/s indicating the presence of wave processes in the deep Black Sea waters.

Another important source of information about the Black Sea currents is mathematical modeling. Multiple simulations of the Black Sea circulation have been

[2] Monin, A.S., Kamenkovich, V.M. and Court, V.G., 1977. *Variability of the World Ocean*. New York: Wiley, 241 p.

conducted using various models [6–13]. Most models simulate key features of large-scale and mesoscale dynamics above the main pycnocline accurately. However, deep currents derived from these models are often described or analyzed in brief only. Moreover, results from different models show significant variability in current velocities and deep-sea circulation direction [11]. Additionally, data assimilation procedures influence simulated current patterns significantly.

Studies [14–16] using the MHI model to simulate deep-sea circulation in the Black Sea focus primarily on currents over the continental slope along the Caucasian coast. In this peripheral the deep-sea region, narrow jet currents opposing the main cyclonic circulation periodically occur. However, deep-sea currents in the central Black Sea remain understudied, despite their higher velocities and greater water layer thickness relative to the periphery.

This study aims to provide a detailed analysis of deep-sea current fields derived from numerical modeling with a two-layer eddy-resolving model incorporating actual bottom topography [17, 18]. Simulations using this model show strong agreement with observed large-scale circulation in the upper layer of the sea. This is attributed to the pronounced density gradient between surface and deep-sea waters, enabling the Black Sea to be modeled as a two-layer system [2]. Given the relatively stable water density below the main pycnocline [1], deep-sea currents derived from this model approximate reality likely closely.

The model incorporates bottom topography, which influences the formation of deep-sea circulation significantly. Furthermore, this simplified model provides a statistically stable solution enabling time-averaged estimates of circulation and current energy parameters.

Materials and methods

Two-layer model. Parameter selection. The model represents a closed water basin comprising two homogeneous fluid layers with different density ($\rho_1 < \rho_2$). The equations of the two-layer model are obtained by integrating the primitive equations of motion and continuity for the upper and lower layers in a Cartesian coordinate system with a downward-directed *Z*-axis:

$$\frac{\partial u_1 h_1}{\partial t} + \frac{\partial u_1^2 h_1}{\partial x} + \frac{\partial v_1 u_1 h_1}{\partial y} - f v_1 h_1 = g h_1 \frac{\partial \zeta}{\partial x} + \tau^x - R_L^x + A_B h_1 \Delta\left(\Delta u_1\right),$$

$$\frac{\partial v_1 h_1}{\partial t} + \frac{\partial u_1 v_1 h_1}{\partial x} + \frac{\partial v_1^2 h_1}{\partial y} + f u_1 h_1 = g h_1 \frac{\partial \zeta}{\partial y} + \tau^y - R_L^y + A_B h_1 \Delta\left(\Delta v_1\right),$$

$$\frac{\partial u_2 h_2}{\partial t} + \frac{\partial u_2^2 h_2}{\partial x} + \frac{\partial v_2 u_2 h_2}{\partial y} - f v_2 h_2 = g h_2 \frac{\partial \zeta}{\partial x} + g' h_2 \frac{\partial h_1}{\partial x} + R_L^x - R_D^x + A_B h_2 \Delta\left(\Delta u_2\right),$$

$$\frac{\partial v_2 h_2}{\partial t} + \frac{\partial u_2 v_2 h_2}{\partial x} + \frac{\partial v_2^2 h_2}{\partial y} + f u_2 h_2 = g h_2 \frac{\partial \zeta}{\partial y} + g' h_2 \frac{\partial h_1}{\partial y} + R_L^y - R_D^y + A_B h_2 \Delta\left(\Delta v_2\right),$$

$$\frac{\partial h_1}{\partial t}+\frac{\partial u_1 h_1}{\partial x}+\frac{\partial v_1 h_1}{\partial y}=0,$$
$$\frac{\partial h_2}{\partial t}+\frac{\partial u_2 h_2}{\partial x}+\frac{\partial v_2 h_2}{\partial y}=0,$$

where $(u_1,v_1),(u_2,v_2)$ are horizontal components of currents in the upper and lower layers, respectively (eastward *X*-axis, northward *Y*-axis); $f=f_0+\beta y$ is Coriolis parameter, $f_0=10^{-4}$ 1/s, $\beta=1.67\cdot10^{-11}$ 1/(m·s); g = 9.81 m/s^2 is gravitational acceleration; $g'=g(\rho_2-\rho_1)/\rho_2$ is reduced gravitational acceleration; ρ_1, ρ_2 are seawater density in the layers; R_L^x, R_L^y are interfacial friction components between layers, $\left\{R_L^x=r_1\left(u_1-u_2\right),\ R_L^y=r_1\left(v_1-v_2\right)\right\}$ when $h_2 > 0$, $\{R_L^x=\left(r_2+r_3\left|\mathbf{u}_1\right|\right)u_1$, $R_L^y=\left(r_2+r_3\left|\mathbf{u}_1\right|\right)v_1\}$ when $h_2 = 0$; R_D^x, R_D^y are bottom friction components in the lower layer $\left\{R_D^x=\left(r_2+r_3\left|\mathbf{u_2}\right|\right)u_2,\ R_D^y=\left(r_2+r_3\left|\mathbf{u_2}\right|\right)v_2\right\}$, r_1, r_2, r_3 are empirical coefficients; A_B is coefficient of horizontal turbulent viscosity; τ^x, τ^y are wind shear stress components; $\Delta=\frac{\partial^2}{\partial x^2}+\frac{\partial^2}{\partial y^2}$ is Laplace operator.

To close the system of equations, the integral continuity equation is applied using the rigid lid approximation:

$$U_x+V_y=0,$$

enabling the introduction of an integral streamfunction ψ at

$$U=-\psi_y,\ V=\psi_x,$$

where $U=u_1h_1+u_2h_2,\ V=v_1h_1+v_2h_2,$ are components of total flow.

Boundary conditions at the sea surface, the interface between layers and seabed are applied in deriving equations (1) – (4). Along the lateral boundaries, no-slip conditions and a zero velocity Laplacian are imposed:

$$u_k=v_k=0,\quad \Delta u_k=\Delta v_k=0,\quad k=1;2.$$

The Coriolis parameter is modeled using the β-plane approximation. The model incorporates bottom friction, friction between layers and horizontal turbulent viscosity modeled with a biharmonic operator. Circulation is driven solely by wind shear stress. Buoyancy fluxes at the sea surface and lateral boundaries are neglected, with buoyancy balanced by two layers of different density where the interface represents a constant pycnocline.

The two-layer model equations are discretized using finite differences on an Arakawa B-grid. Divergent terms in the equations of motion and continuity are discretized with central differences, and a semi-implicit scheme is employed for time integration [19].

In this study's experiments, the horizontal grid step and time integration step were $\Delta x = \Delta y = 2$ km and $\Delta t = 120$ s, respectively. For this time step, biharmonic turbulent viscosity coefficient $A_B = 1.5 \cdot 10^8$ m⁴/s was selected to ensure numerical stability.

Other model parameters were calibrated to observed Black Sea conditions. The reduced gravity acceleration $g' = g(\rho_2 - \rho_1)/\rho_2$ derived from the density difference between layers corresponding to a salinity difference ($\Delta S = 4$ ‰), was set to 0.032 m/s². The upper layer thickness at rest was set to $h_0 = 100$ m.

Bottom friction is modeled as proportional to the square of current velocity, with the friction coefficient calibrated to match observed deep-sea current velocities from [4, 5].

Model fields of wind shear stress on the sea surface were derived from empirical formulas accounting for spatial and temporal variability of observed wind fields [20]. The annual mean wind stress vorticity was consistent with observed values [1].

Spatially averaged kinetic energy values were used to monitor the numerical experiments in the upper $\langle K_1 \rangle$ and lower $\langle K_2 \rangle$ layers, defined by formulas

$$\langle K_1 \rangle = \rho \left\langle h_1 \frac{u_1^2 + v_1^2}{2} \right\rangle, \quad \langle K_2 \rangle = \rho \left\langle h_2 \frac{u_2^2 + v_2^2}{2} \right\rangle,$$

where angle brackets denote spatial averaging over the entire sea area; (u_1, v_1), (u_2, v_2) are horizontal velocity components in the upper and lower layers, respectively; h_1, h_2 represent layer thickness; ρ is mean sea water density.

Results of numerical experiments

The spatial and temporal variability of deep-sea current fields was analyzed using three numerical experiments (E1, E2, E3) conducted with the two-layer model. These experiments differed only in the amplitude and temporal variability of surface wind stress. In all experiments, calculations began from a state of rest, with the sea surface and interface between layers assumed horizontal and current velocities set to zero.

In experiment E1, the surface wind stress field was temporarily constant but incorporated spatial distribution features [20]. As demonstrated in [21], these features are critical for the accurate development of large-scale circulation. Experiment E1 aimed to trace the evolution of circulation from a state of rest to statistical equilibrium. Furthermore, the experiments revealed that under stationary external forcing conditions, the model reached statistical equilibrium faster. Algorithmically, constant wind stress field $\boldsymbol{\tau}$ $(x, y) = (\tau^x, \tau^y)$ was derived from the following formulas:

$$\tau^x(x,y) = -\tau_0^x \cos\left(\frac{\pi x}{L} + \pi\left(\frac{1}{2} - \alpha S\right)\right)\cos\left(\frac{\pi y}{B}\right)(1-S),$$
$$\tau^y(x,y) = -\tau_0^y \sin\left(\frac{\pi x}{L} + \pi\left(\frac{1}{2} - \alpha S\right)\right)(1-S)\left(\frac{(x/\Delta x)^2 + 20000}{(L/\Delta x)^2 + 20000}\right), \quad (1)$$

where τ_0^x, τ_0^y are constant amplitude values; $\alpha \in [0;1]$ is coefficient determining eastward propagation of anticyclonic vorticity zone; $S \in [0;\ 0.5]$ is parameter controlling temporal variability.

Fig. 1 shows the spatial distributions of fields $\boldsymbol{\tau}$ and $\mathrm{rot}_Z\ \boldsymbol{\tau}$ obtained in experiment E1. The calculation of $\boldsymbol{\tau}$ in equation (1) used the following parameters: $\tau_0^x = \tau_0^y = 0.05$ N/m^2, $\alpha = 0.85$, $S = 0.4$. Fig. 1 indicates maximum positive vorticity $\boldsymbol{\tau}$ (corresponding to a cyclone) in the eastern Black Sea and negative vorticity (anticyclonic) in the western Black Sea.

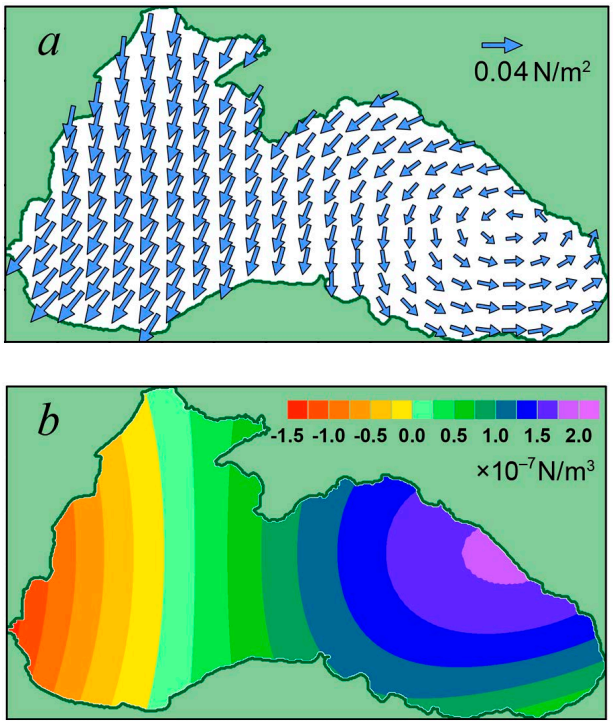

F i g. 1. Stationary fields $\boldsymbol{\tau}$ (*a*) and $\mathrm{rot}_Z\ \boldsymbol{\tau}$ (*b*) in experiment E1

Graphs of temporal variability $\langle K_1 \rangle$ and $\langle K_2 \rangle$ constructed for experiment E1 (Fig. 2, *a*, *b*) show that during the first year from the start of the calculations, the kinetic energy of the currents increases both in the upper and lower sea layers. At this time, under effect of the wind with cyclonic vorticity, the RC jet forms in the upper layer, which is located to the left of the distribution boundary of the lower (deep-water) layer (Fig. 3, *a*1). In the lower layer, Ekman pumping [22] drives the currents primarily along the isobaths (Fig. 3, *b*1).

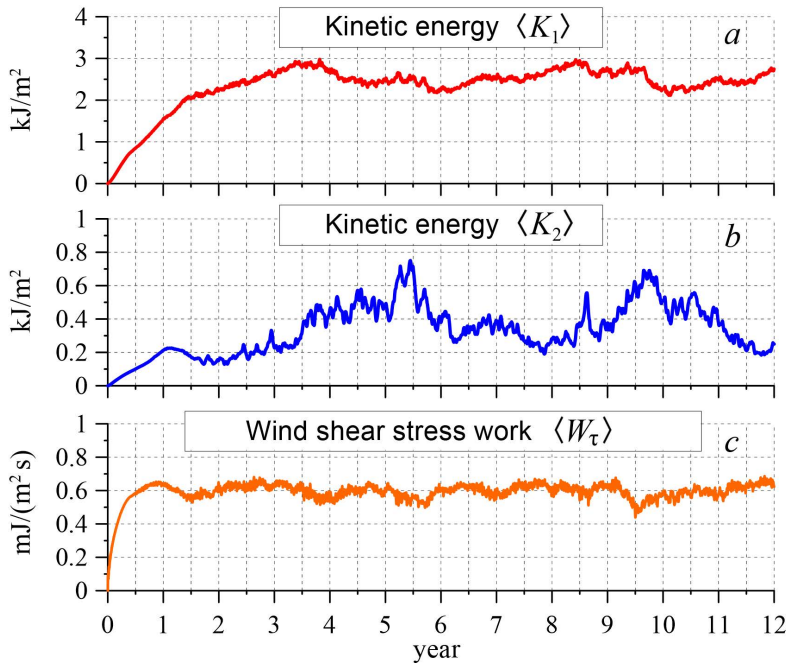

F i g. 2. Time dependence of $\langle K_1 \rangle$ (*a*), $\langle K_2 \rangle$ (*b*) and $\langle W_\tau \rangle$ (*c*) in experiment E1

Near the current velocity fields (Fig. 3, *a*1, *b*1), corresponding sea level ζ and function *M* fields are given (Fig. 3, *a*2, *b*2). Function *M* (similar to Montgomery potential in meteorology) represents the water pressure in the lower layer while ζ represents the pressure in the upper layer.

Scalar fields ζ and *M* facilitate visualization of currents as alternatives to vector fields u_1, u_2. Under geostrophic equilibrium, ζ isolines represent streamlines for upper-layer currents while *M* isolines represent streamlines for lower-layer currents with higher values of ζ and *M* to the right of the flow direction. The current velocity increases with decreasing spacing of ζ or *M* isolines.

To facilitate comparison of currents between layers, ζ isolines corresponding to the RC core are superimposed on the *M* maps in pink.

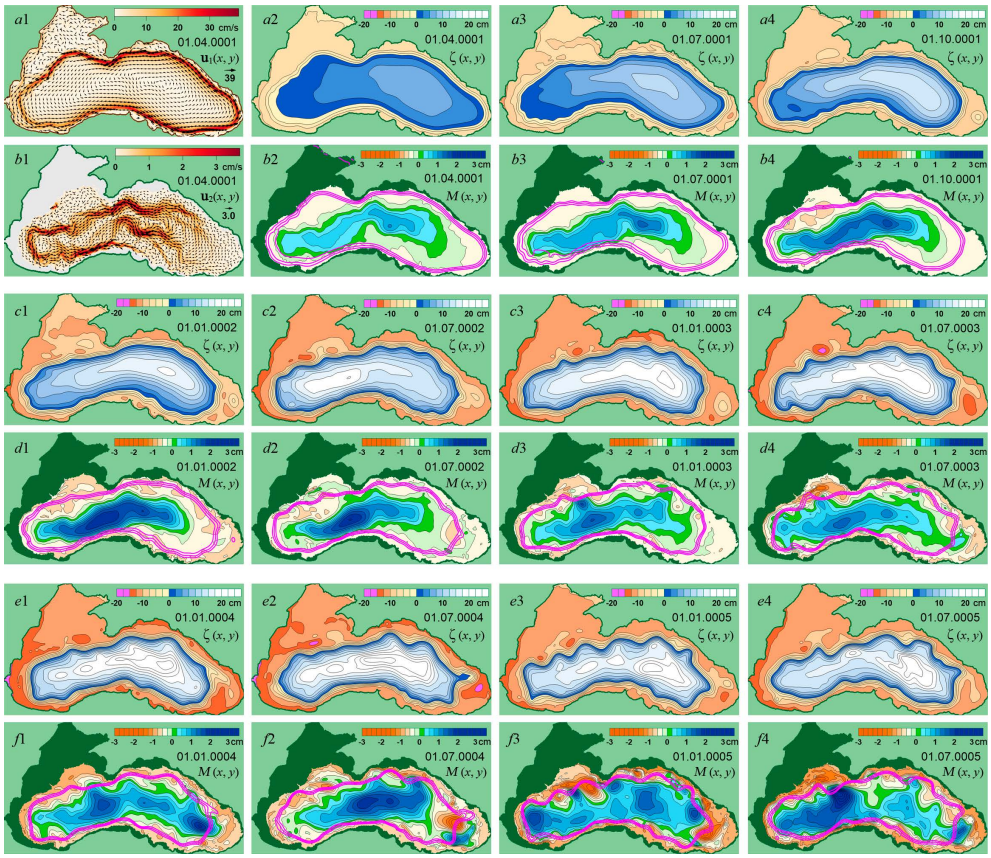

F i g. 3. Instantaneous fields u_1 (*a*1), u_2 (*b*1), ζ (*a*2 – *a*4, *c*1 – *c*4, *e*1 – *e*4) and M (*b*2 – *b*4, *d*1 – *d*4, *f*1 – *f*4) in experiment E1

Maps $\zeta(x, y)$ and $M(x, y)$ dated 01.07.0001–01.01.0002 (Fig. 3, *a*3, *a*4, *b*3, *b*4, *c*1, *d*1) demonstrate that currents in both upper (RC) and lower layers intensify during the first year, leading to increasing values of $\langle K_1 \rangle$ and $\langle K_2 \rangle$ (Fig. 2, *a*, *b*).

During the second year, the RC strengthens (Fig. 3, *c*2 – *c*4) and $\langle K_1 \rangle$ increases while circulation weakens (Fig. 3, *d*2 – *d*4) and $\langle K_2 \rangle$ decreases in the lower layer. This behavior results from a decrease in wind shear stress work $\langle W_\tau \rangle$ after its peak at the end of the first year (Fig. 2, *c*). Consequently, the uplift of the interface between layers driven by Ekman pumping slows down. The decrease in $\langle W_\tau \rangle$ is in turn associated with the alignment of the RC jet in the eastern Black Sea and its displacement from the region of maximum wind stress vorticity (Fig. 3, *a*4).

By the end of the second year, the wind energy input into the sea stabilizes at a steady level until the calculations end (Fig. 2, *c*) indicating a statistical equilibrium regime. The stabilization of $\langle W_\tau \rangle$ stems from increased velocity of surface currents and the onset of RC instability manifested through its meandering, which begins around the sixth month of the first year and evolves throughout the second and third years (Fig. 3, *a*3, *a*4, *c*1 – *c*4).

The intensified RC instability leads to the formation of eddy structures (ES) [3] at the periphery of the lower layer (beneath the RC). These structures move along the continental slope with cyclonic motion, aligned with the RC meandering (Fig. 3, *d*1 – *d*4, *f*1 – *f*4). This process is most pronounced in the northern Black Sea.

During the third and fourth years, the kinetic energy of currents increases in both layers (Fig. 2, *a*, *b*). In the lower layer, this energy growth results from the growing number and size of eddy structures forming along the continental slope and continental rise. By the fifth year, eddy formation in the lower layer reaches its peak (Fig. 3, *f*3) corresponding to the level of wind energy input under statistical equilibrium conditions.

The eddy structures emerging in the lower layer represent traveling waves in the current field, classified as gradient-vorticity waves [23] due to the conservation of potential vorticity [24]. For the lower layer of a two-layer fluid, this conservation law takes the following form:

$$\frac{d}{dt}\frac{f+\xi_2}{H}=0 \quad \text{or} \quad \frac{f+\xi_2}{H}=\text{const},$$

where $\xi_2=\frac{\partial v_2}{\partial x}-\frac{\partial u_2}{\partial y}$ is relative vorticity of current velocity in the lower layer.

According to this law, when a water mass moves, changes in the Coriolis parameter f or sea depth H (x, y) alter relative vorticity ξ_2 of the moving water. In the first case, planetary Rossby waves form, while in the second case, bottom-trapped topographic Rossby waves develop, with the continental slope and continental rise acting as the inclined topography.

Through the analysis of experiments E2 and E3, we examine the characteristics of deep circulation formation under statistical equilibrium conditions. These experiments used wind stress field $\boldsymbol{\tau}$ (x, y, t) with spatial and seasonal variability, achieved by specifying parameter S in equations (1) as a time-dependent function:

$$S(t)=0.5\cdot\sin^2\left(\frac{\pi}{8640}\cdot t\right),$$

where t is time in hours.

The wind stress intensity was adjusted by varying different amplitude values τ_0^x, τ_0^y in equations (1). In experiment E2, these values were set to 0.02 N/m², producing a basin-averaged annual mean wind stress vorticity $\overline{\langle \mathrm{rot}_Z \boldsymbol{\tau} \rangle}$ = $3.8\cdot10^{-8}$ N/m³. For experiment E3, reduced values τ_0^x, τ_0^y equal to 0.015 N/m², at which $\overline{\langle \mathrm{rot}_Z \boldsymbol{\tau} \rangle}$ = $2.6\cdot10^{-8}$ N/m³, were implemented. Both experiments maintained $\alpha = 0.75$.

[3] Ginzburg, A.I., Zatsepin, A.G., Kostianoy, A.G., Krivosheya, V.G., Skirta, A.Yu., Soloviev, D., Stanichny, S., Sheremet, N.A., Shiganova, T.A. [et al.], 2001. Anticyclonic Eddies in the Deep Eastern Black Sea in Summer-Autumn 1999 (Satellite and Ship-Borne Observations). *Issledovanie Zemli iz Kosmosa*, (5), pp. 3-11 (in Russian).

Varying wind stress intensities in experiments E2 and E3 was motivated by the existence of two distinct regimes of large-scale circulation in the Black Sea. As demonstrated in [25], the basin circulation exhibits a bimodal response to wind stress intensity. The first circulation regime emerges when the annual mean wind stress vorticity over the entire sea surface $T = \overline{\langle \mathrm{rot}_Z \boldsymbol{\tau} \rangle}$ exceeds threshold value T_{thr}. In this regime, the RC maintains a stable trajectory along the continental slope, forming continuous cyclonic circulation that encompasses the entire perimeter of the deep-sea basin. Conversely, when $T = \overline{\langle \mathrm{rot}_Z \boldsymbol{\tau} \rangle}$ falls below the threshold T_{thr}, the system transitions to the second circulation regime, characterized by periodic detachment (every 7–10 years) of the RC eastern branch from the coastline and its westward migration. This reorganization shifts the primary cyclonic gyre confining it primarily to the western Black Sea. This transition highlights the nonlinear response of the Black Sea dynamics to variations in atmospheric forcing.

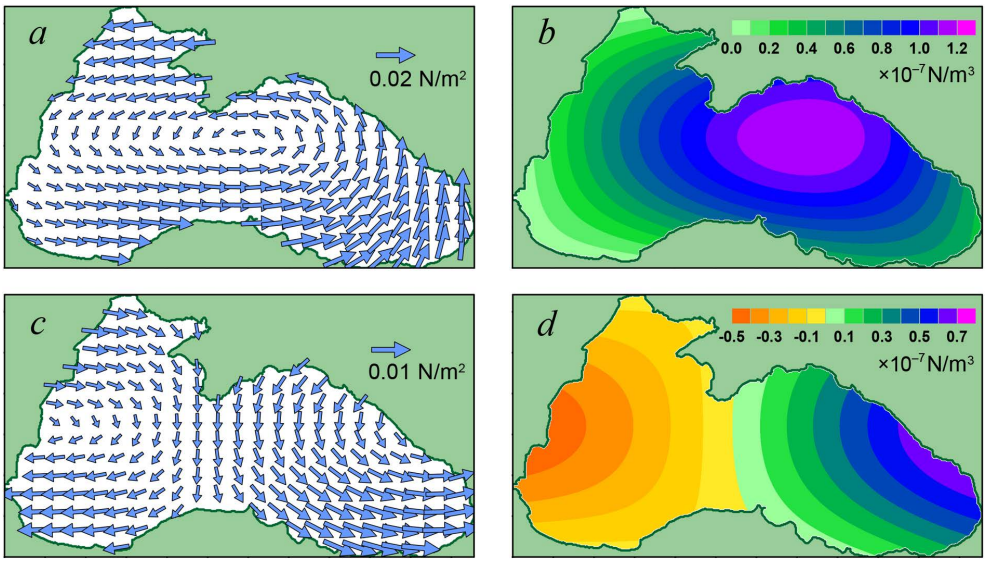

F i g. 4. Fields $\boldsymbol{\tau}$ and $\mathrm{rot}_Z\,\boldsymbol{\tau}$ in experiment E2 in January (*a*, *b*) and July (*c*, *d*)

Fig. 4 shows fields $\boldsymbol{\tau}$ and $\mathrm{rot}_Z\,\boldsymbol{\tau}$ for January 1st and July 1st in experiment E2. During winter months, cyclonic vorticity $\boldsymbol{\tau}$ dominates over the entire sea surface, peaking in the eastern Black Sea. In the first half of the year, this vorticity maximum shifts eastward gradually, while an area of anticyclonic $\boldsymbol{\tau}$ vorticity emerges in the western Black Sea. The second half of the year shows an opposite progression of $\boldsymbol{\tau}$ and $\mathrm{rot}_Z\,\boldsymbol{\tau}$ patterns, with the vorticity features shifting westward.

Graphs in Fig. 5 *a*, *b*, *c* illustrate the temporal evolution of $\langle K_1 \rangle(t)$, $\langle K_2 \rangle(t)$ and $\langle W_\tau \rangle(t)$ in experiment E2. The seasonal variability of wind stress fields drives corresponding oscillations in both wind energy input $\langle W_\tau \rangle$ and upper-layer

circulation intensity, as quantified by $\langle K_1 \rangle$. Notably, the seasonal cycle $\langle K_1 \rangle$ exhibits a phase lag of approximately three months relative to $\langle W_\tau \rangle$ variations, due to the inertial response of the dynamical system.

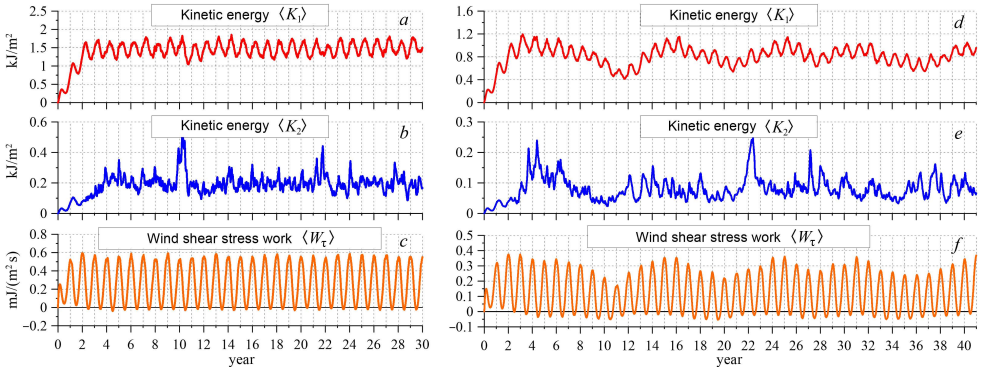

F i g. 5. Graphs of kinetic energy and work of wind shear stress in experiments E2 (*a, b, c*) and E3 (*d, e, f*)

The basin-averaged kinetic energy of lower-layer currents $\langle K_2 \rangle$ exhibits pronounced temporal variability (Fig. 5, *b*), with many energy peaks coinciding with maxima in wind energy input $\langle W_\tau \rangle$. However, establishing a direct correlation between $\langle K_2 \rangle$ and the seasonal cycles of either $\langle W_\tau \rangle$ or upper-layer energy $\langle K_1 \rangle$ would be methodologically unsound. Comparing the temporal evolution of $\langle K_1 \rangle$ and $\langle K_2 \rangle$ (Fig. 5 *a*, *b*) requires accounting for their distinct scale ranges and spatially averaged nature.

The circulation dynamics in the upper and lower layers can be traced through the sequential ζ (x, y) and M (x, y) fields shown in Fig. 6. The upper two rows demonstrate winter season, while the lower two rows depict summer months. In M field panels, additional ζ isolines marking the RC core are superimposed. The analysis reveals greater stability of the RC in the upper layer during winter months, indicated by fewer and smaller meanders compared to July when meanders are more frequent.

In the lower layer, January exhibits stronger currents in the central part of the deep-sea basin compared to July (Fig. 6, *b*1–*b*4, *d*1–*d*4), likely driven by enhanced Ekman pumping during winter. The propagation of more energetic eddies along the northeastern continental slope and continental rise contributes further, with eddies forming in the southeastern Black Sea near Trabzon, weakening as they move toward the Crimean Peninsula, and regaining intensity to strengthen currents in the western deep-sea basin (Fig. 6, *b*3, *b*4). The summer period demonstrates similar but weaker patterns of eddy generation and propagation along the northern continental slope.

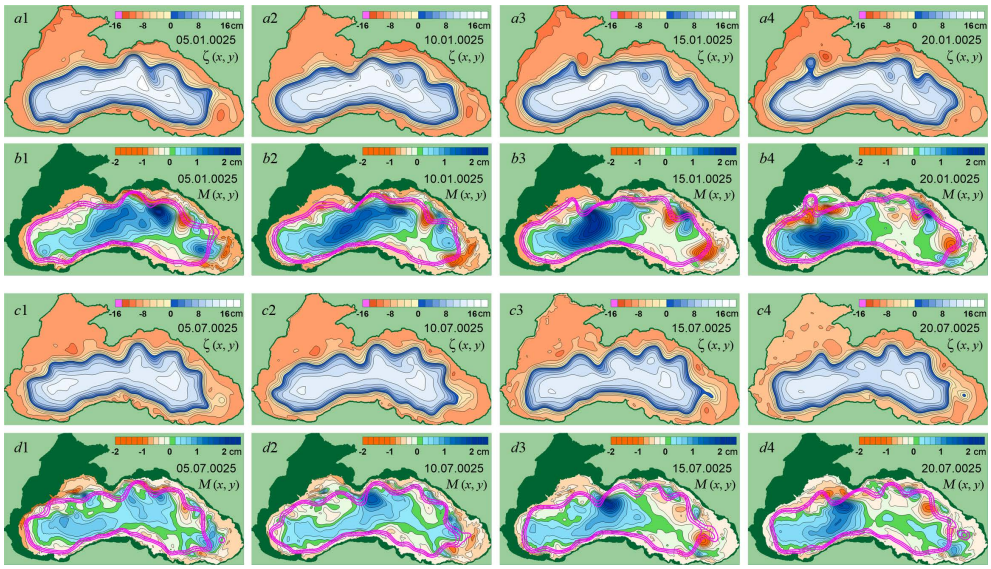

F i g. 6. Instantaneous fields ζ (*x, y*) and *M* (*x, y*) in experiment E2

During the summer period, eddies along the northern continental slope exhibit patterns of generation, propagation and transformation similar to those in winter months, but with lower intensity (Fig. 6, *d*3, *d*4).

Visual comparison of the RC jet position with lower-layer eddies (Fig. 6, *b*1–*b*4, *d*1–*d*4) reveals a consistent correlation. Typically, the RC jet shifts seaward over cyclonic eddies, while moving shoreward over anticyclonic ones. The phase propagation velocities of both RC meanders and eddies show complete synchrony.

In experiment E3, as previously mentioned, the wind stress field exhibited mean annual vorticity $T = \overline{\langle \mathrm{rot}_Z \boldsymbol{\tau} \rangle}$ below threshold value T_{thr} across the sea area, inducing distinct 7–9-year oscillations in circulation intensity, as shown in Fig. 5, *d*. In the $\langle K_2 \rangle$ graph (Fig. 5, *e*), no oscillations similar to $\langle K_1 \rangle$ are observed. However, significant amplitude spikes occurring predominantly during winter take place. As explained in [25], the $\langle K_1 \rangle$ oscillations result from variations in wind energy input $\langle W_\tau \rangle$ caused by the RC east-to-west displacement. The $\langle K_1 \rangle$ maxima correspond to periods when the RC flows along the entire perimeter of the deep-sea zone while $\langle K_1 \rangle$ minima occur when the it crosses the central Black Sea.

Fig. 7 presents the instantaneous ζ (*x*, *y*) and *M* (*x*, *y*) fields obtained in experiment E3. The upper two rows of panels correspond to periods when $\langle K_1 \rangle$ reaches maximum values when the circulation pattern resembles that in experiment E2 (Fig. 6, *d*1–*d*4).

The third and fourth rows in Fig. 7 show fields characteristic of periods with minimum $\langle K_1 \rangle$ values. During these phases, the RC demonstrates an anomalous cross-basin trajectory crossing connecting the Turkish coastal waters and the Novorossiysk area through the central eastern deep-sea basin. This displacement

from the eastern and northeastern Black Sea continental slope weakens lower-layer deep-sea circulation and halts eddy generation in the southeastern Black Sea.

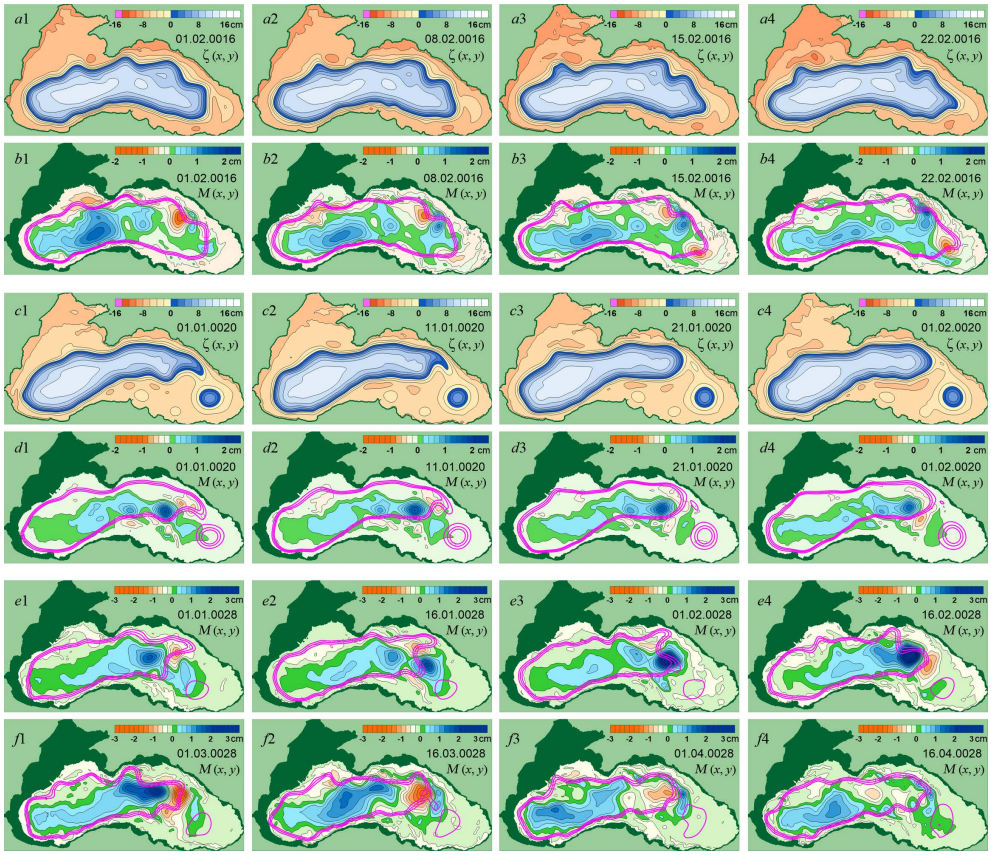

F i g. 7. Instantaneous fields ζ (*x, y*) and *M* (*x, y*) in experiment E3

The bottom two rows of Fig. 7 show the $\zeta(x, y)$ and $M(x, y)$ fields corresponding to the sharp intensification of $\langle K_2 \rangle$ observed in early February, year 28 (from the beginning of the calculations) (Fig. 5, *e*). This $\langle K_2 \rangle$ spike results from a strong cyclonic eddy forming and intensifying over the continental rise near the Caucasian coast (Fig. 7, *e*3, *e*4). After peaking, the eddy propagates along the continental rise, strengthening the cyclonic circulation in the western deep-sea basin.

The $\langle K_2 \rangle$ spikes resulting from intensifying eddies are a key characteristic of lower-layer dynamics. These energetic events manifest as direct consequences of hydrodynamic instability in large-scale currents. A detailed examination of the mechanisms generating lower-layer circulation will be explored in future research.

The features of the spatial distribution of currents in the lower layer of the sea obtained in the two-layer model show good agreement with modeling results in

[14, 15]. However, those studies do not analyze the dynamics of deep currents or explain the causes of eddy formation in the lower layer of the Black Sea adequately.

Mean and eddy currents

To analyze dynamic processes in the sea, we applied a statistical method, which consists in dividing real (instantaneous) currents into mean and deviations from the mean (pulsations). Visually, current pulsations most often have an eddy structure, so they are also called eddy currents. An important point in dividing currents into mean and eddy is the choice of the averaging period, which is determined based on the tasks and specific dynamics of the sea. When analyzing mean and eddy currents, it is necessary to remember that such a division is conceptual, as only total currents exist in reality.

We examine the results of applying statistical analysis to experiment E2. In the layered model, the flow is defined as the product of current velocity and layer thickness. This is expressed as $\mathbf{U}_1 = \mathbf{u}_1 h_1$ for the upper layer and $\mathbf{U}_2 = \mathbf{u}_2 h_2$ for the lower layer. Then mean currents are calculated as $\mathbf{U}_1^{\mathrm{m}} = \overline{\mathbf{u}_1 h_1}$, $\mathbf{U}_2^{\mathrm{m}} = \overline{\mathbf{u}_2 h_2}$, with deviations from the mean (pulsations) $\mathbf{U}_1^{\mathrm{p}} = \mathbf{U}_1 - \mathbf{U}_1^{\mathrm{m}}$, $\mathbf{U}_2^{\mathrm{p}} = \mathbf{U}_2 - \mathbf{U}_2^{\mathrm{m}}$. The overbar means averaging over time, superscript "m" is used to denote mean currents, "p" – for pulsations. We set the averaging period to be long enough (at least 20 years) to exclude temporal variability of mean currents.

Fig. 8 presents the fields of mean and eddy currents in the upper layer (first row) and lower layer (third row), along with their corresponding ζ (second row) and M (fourth row) fields. Mean current fields $\mathbf{U}_1^{\mathrm{m}}, \zeta^{\mathrm{m}}, \mathbf{U}_2^{\mathrm{m}}, M^{\mathrm{m}}$ are given in the first column, while columns two to four display eddy current fields $\mathbf{U}_1^{\mathrm{p}}, \zeta^{\mathrm{p}}, \mathbf{U}_2^{\mathrm{p}}, M^{\mathrm{p}}$.

The upper-layer mean currents propagate along the continental slope deviating from isobaths and follow sea surface isolines consistent with geostrophic balance. The core velocities of mean currents reach 20 cm/s and a flow width of 30–50 km. Over a 20-year averaging period, mean currents remain nearly stationary in both upper and lower layers.

Visually, upper-layer current oscillations appear as alternating cyclonic and anticyclonic eddies propagating counterclockwise along the mean RC core (cyclonic rotation). These eddies exhibit significantly larger amplitude in the northern Black Sea compared to the southern region. Upper-layer eddy generation and the RC meanders in the western boundary current both result from the hydrodynamic instability of the large-scale flow.

Lower-layer mean currents are strongly influenced by bathymetry, with streamlines (represented by M^{m} isolines) closely following isobaths.

The oscillating (eddy) component of deep currents similarly consists of alternating mesoscale eddy structures propagating cyclonically over the continental slope and continental rise. The likely generation mechanisms for these eddies include the RC instability, topographic and planetary β-effects.

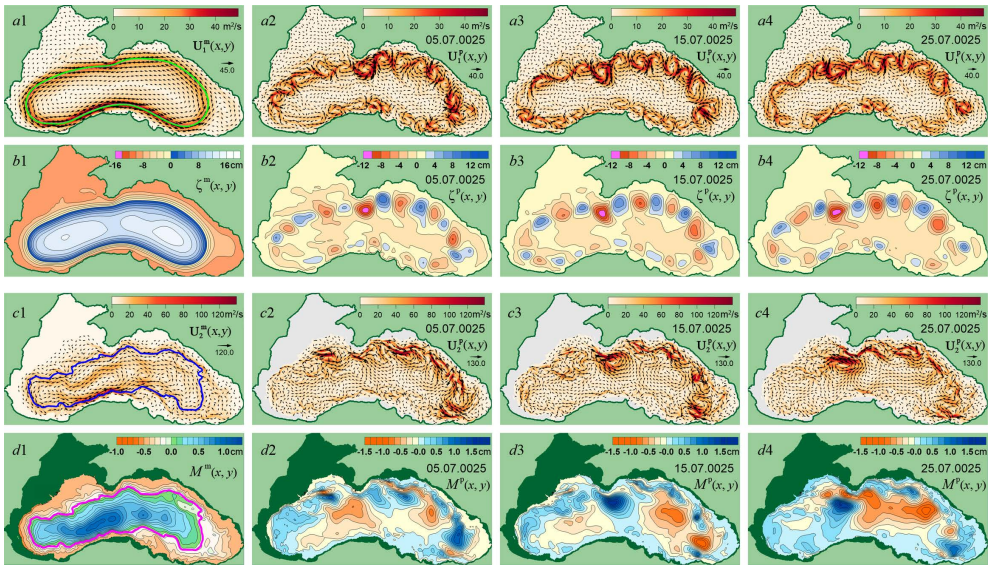

F i g. 8. Mean fields $\mathbf{U}_1^{\mathrm{m}}$ ($a1$), ζ^{m} ($b1$), $\mathbf{U}_2^{\mathrm{m}}$ ($c1$), M^{m} ($d1$) and instantaneous fields $\mathbf{U}_1^{\mathrm{p}}$ ($a2 – a4$), ζ^{p} ($b2 – b4$), $\mathbf{U}_2^{\mathrm{p}}$ ($c2 – c4$), M^{p} ($d2 – d4$) in experiment E2

Visually, the fields of eddy and instantaneous currents in the lower layer show strong similarity indicating a dominant eddy component in the total flow. To confirm this, we calculate the spatially averaged kinetic energy of mean $K_1^{\mathrm{m}}, K_2^{\mathrm{m}}$ and eddy $K_1^{\mathrm{p}}, K_2^{\mathrm{p}}$ components in the upper and lower layers:

$$\overline{K_1} = \sum_S \rho \frac{\overline{h_1 \mathbf{u}_1^2}}{2} = K_1^{\mathrm{m}} + K_1^{\mathrm{p}}, \quad K_1^{\mathrm{m}} = \sum_S \rho \frac{\mathbf{U}_1^{\mathrm{m}} \cdot \overline{\mathbf{u}_1}}{2}, \quad K_1^{\mathrm{p}} = \overline{K_1} - K_1^{\mathrm{m}},$$

$$\overline{K_2} = \sum_S \rho \frac{\overline{h_2 \mathbf{u}_2^2}}{2} = K_2^{\mathrm{m}} + K_2^{\mathrm{p}}, \quad K_2^{\mathrm{m}} = \sum_S \rho \frac{\mathbf{U}_2^{\mathrm{m}} \cdot \overline{\mathbf{u}_2}}{2}, \quad K_2^{\mathrm{p}} = \overline{K_2} - K_2^{\mathrm{m}}.$$

After averaging over the area, we obtain the following values:

$$\left\langle \overline{K_1} \right\rangle = 1.46 \text{ kJ/m}^2, \quad \left\langle K_1^{\mathrm{m}} \right\rangle = 1.04 \text{ kJ/m}^2 \ (71\%), \quad \left\langle K_1^{\mathrm{p}} \right\rangle = 0.42 \text{ kJ/m}^2 (29\%),$$

$$\left\langle \overline{K_2} \right\rangle = 0.20 \text{ kJ/m}^2, \quad \left\langle K_2^{\mathrm{m}} \right\rangle = 0.07 \text{ kJ/m}^2 (34\%), \quad \left\langle K_2^{\mathrm{p}} \right\rangle = 0.13 \text{ kJ/m}^2 (66\%).$$

Thus, the mean component accounts for 71% of the energy in the upper layer, with the eddy component contributing 29%. Conversely, in the lower layer, the eddy component dominates, accounting for 66% of energy, while the mean component contributes 34%.

Interestingly, decomposition into mean and eddy components reveals coherent eddies coinciding with the RC meanders in the upper layer. In contrast, averaging reveals mean deep currents following isobaths that remain visually obscured in instantaneous fields.

Parameters of wave oscillations of deep currents

To study the dispersion properties of wave processes in deep current fields, we constructed temporal variability diagrams of current characteristics along wave propagation trajectories.

As gradient-eddy waves involve oscillations of the horizontal current vector, the transverse component of the current velocity is a logical choice for constructing diagrams. However, since geostrophic balance governs large-scale and mesoscale dynamic processes, the fields $M(x, y, t)$ from experiment E2 were used as input data.

The core of the mean current, defined as the streamline with maximum flow velocity (Fig. 9, *a*), was selected as the reference level. Due to the geostrophic nature of the mean currents, zero isoline M^{m}, corresponding to this flow core, was used as the reference level (Fig. 8, *d*1), closely following the isobath at H = 1950 m (Fig. 9, *b*). Note that bathymetry results in several cores in the mean flow field.

To facilitate correlation between the temporal variability diagram and the Black Sea map, reference points were marked on it at regular intervals (Fig. 9, *a*).

Fig. 9, *c* demonstrates a high-resolution (1-day sampling) temporal variability diagram M^{p} along the zero isoline M^{m} over model years 23–25. Vertical dashed lines, numbered along the top axis, correspond to reference points shown in Fig. 9, *a*.

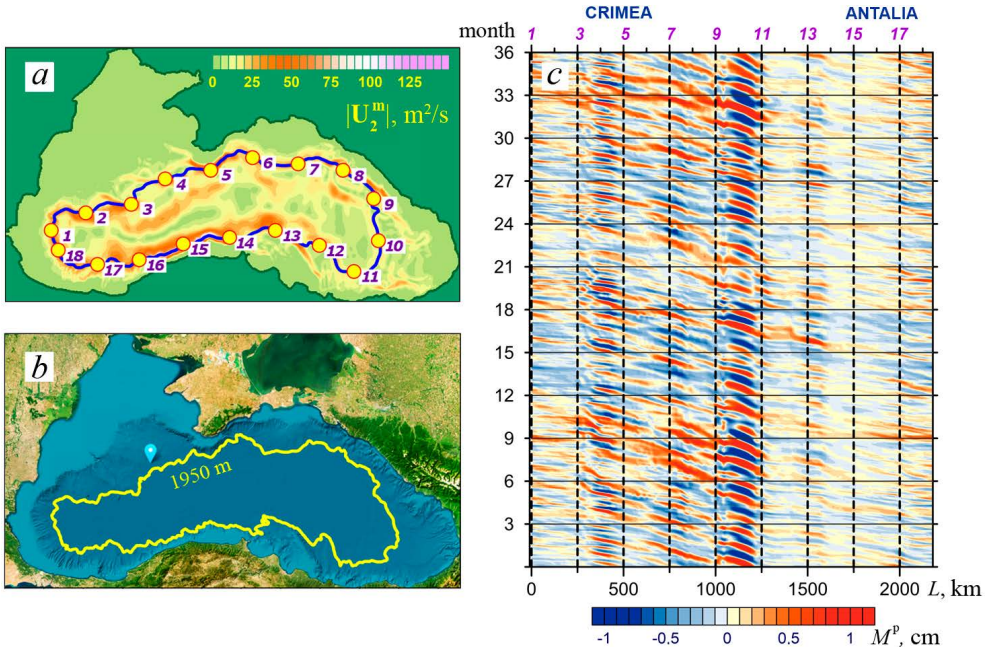

F i g. 9. Modulus of mean flow in the lower layer $\left|\mathbf{U}_2^{\mathrm{m}}\right|$ (*a*), isobath H = 1950 m (*b*), and time diagram M^{p} along isobaths M^{m} (*c*)

The diagram shows alternating oscillations in M^{p}, indicating wave motion along the selected trajectory in a counterclockwise direction. The phase velocity of these waves can be estimated from the slope of lines connecting identical oscillation phases, with notable variations across different segments of the trajectory. The fastest wave propagation occurs between reference points 18–11 in the southern part of the trajectory.

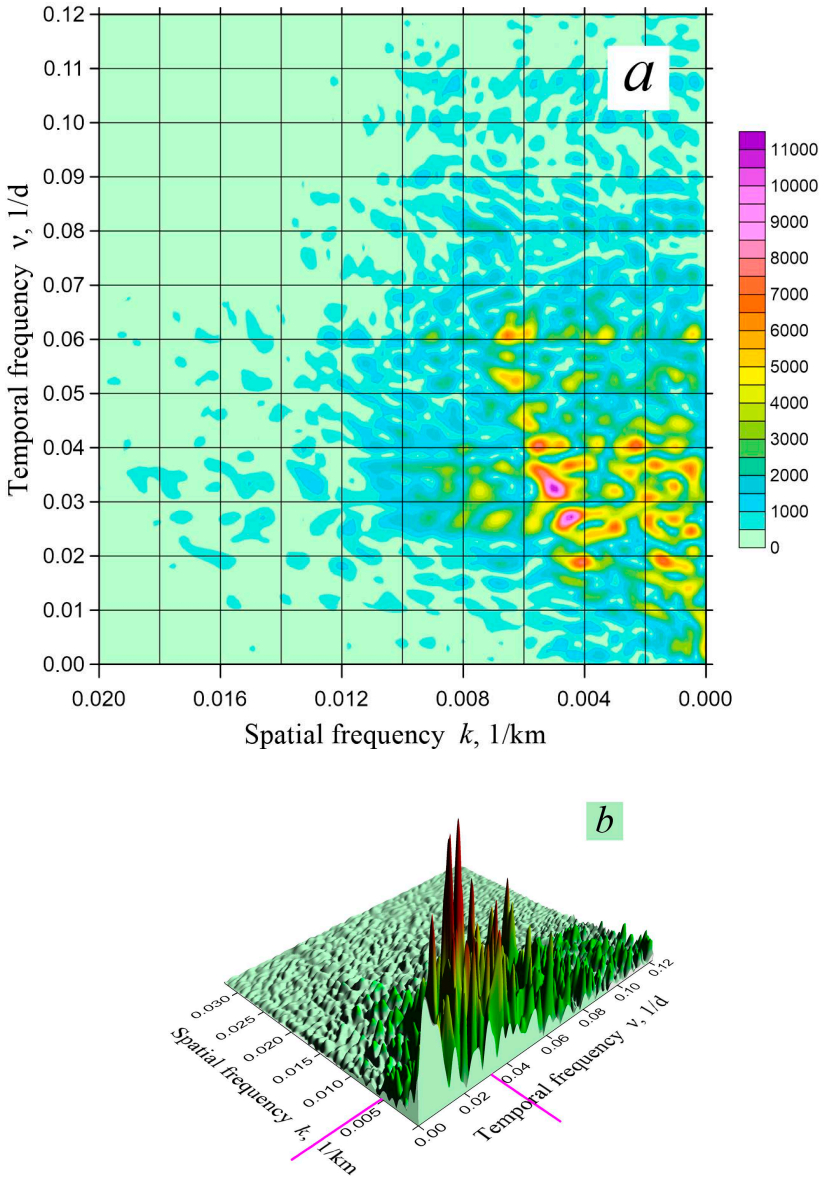

F i g. 10. Two-dimensional spectrum of wave oscillations in the field of deep currents in 2D (*a*) and 3D (*b*) formats

Wave activity intensifies significantly between reference points 11–9 in the eastern Black Sea, a generation zone for topographic Rossby waves (Figs. 6, 8). Additionally, amplified wave amplitudes occur between points 5 and 3 along the segment extending south of the Crimean Peninsula and westward.

The second stage of analyzing dispersion characteristics of wave oscillations involved computing a two-dimensional wave spectrum from the diagram (Fig. 9, *c*) using Fast Fourier Transform (FFT). The time diagram is a data array of 1080 daily samples of function M along trajectory L with a 2 km resolution.

Fig. 10 shows two-dimensional (in frequency and spatial frequency) spectrum $S = f(\nu, k)$ in 2D and, for clarity, 3D formats.

As we can see from Fig. 10, wave processes in the deep currents have the ranges of 0.01–0.06 1/day in frequency and 0.005–0.08 1/km in spatial frequency, corresponding to waves with periods of 17–100 days and lengths of 12–200 km. Such waves are classified as long as their shortest wavelength in the interval is several times greater than the sea depth.

The considerable variability in wave dispersion characteristics can be attributed to changing bottom slope along their propagation trajectory and multiple wave generation mechanisms. Nevertheless, the obtained dispersion properties, combined with observed wave features (vortical character, propagation direction and topographic dependence), align with previously identified waves trapped by the continental slope, accounting for planetary β-effects.

The derived spectrum shows peak energy concentration in waves with frequency ν = 0.033 cycles/day and wavenumber k = 0.0051 cycles/km, corresponding to wavelengths λ = 196 km and periods T = 30 days. These waves propagate along the selected trajectory (Fig. 9, *a*) with phase velocity C_{ph} = 0.078 m/s. Similar dispersion characteristics were previously reported in [26] concerning the RC meanders near Gelendzhik.

It should be emphasized that the analyzed spectrum (Fig. 10) only represents wave characteristics along a single trajectory. Spectral properties would likely differ for other trajectories across the region. Different wave dispersion characteristics can also be obtained for different sections of the same trajectory.

Conclusion

This study concludes that deep circulation in the Black Sea represents a combination of alternating eddy structures and mean currents flowing approximately along isobaths. These eddy formations propagate cyclonically (counterclockwise) around the deep-sea perimeter as long waves, with dispersion characteristics matching those of waves trapped by the Black Sea bathymetry comprising the continental slope and continental rise.

Eddy formations are the primary component of deep circulation, accounting for two-thirds of the kinetic energy of deep currents. In contrast, eddy currents in the upper layer contribute only one-third of the kinetic energy.

Deep circulation in the Black Sea exhibits a persistent cyclonic (counterclockwise) pattern, with both propagating phases of trapped topographic Rossby waves and mean currents following this dominant rotation. The observed phase velocities of long waves exceed the velocities of mean currents significantly.

Two possible sources generate deep currents in the Black Sea. Ekman pumping, a wind-driven mechanism, induces geostrophic currents. In the two-layer model, Ekman pumping manifests itself in the rise of the layer interface, which leads to the occurrence of currents in the lower (deep-sea) layer. Additionally, the RC instability generates eddy disturbances in both upper and lower sea layers.

The obtained results identify two distinct regions in the Black Sea where the formation and/or intensification of long waves occurs. These regions are located in the eastern Black Sea near Trabzon and southwest of the Crimean Peninsula.

This study of deep circulation raises several unresolved questions of significant scientific interest. First, the spatial distribution of dispersion characteristics of long waves remains unexplored. Second, the mechanisms of deep current generation require further investigation. Third, the relative influence of Rim Current instability, planetary β-effect and topographic β-effect on the formation of eddy waves in the deep sea needs quantification. These questions will be addressed in subsequent studies.

A further question concerns the agreement between the current pattern presented here for the lower layer and the observed circulation in the deep Black Sea. This requires validation through appropriate field experiments.

REFERENCES

1. Ivanov, V.A. and Belokopytov, V.N., 2013. *Oceanography of the Black Sea*. Sevastopol: ECOSI-Gidrofizika, 210 p.
2. Konovalov, S.K., Vidnichuk, A.V. and Orekhova, N.A., 2018. Spatio-Temporal Characteristics of the Hydrochemical Structure of Water in the Deep-Sea Part of the Black Sea. In: A.P. Lisitzin, ed., 2018. The *Black Sea System*. Moscow: Scientific World, pp. 106-119. https://doi.org/10.29006/978-5-91522-473-4.2018.106 (in Russian).
3. Ivanov, V.A., Plastun, T.V., Markova, N.V. and Bagaev, A.V., 2019. Statistical Parameters of the Black Sea Deep Currents Based on Measurement Data. *Fundamental and Applied Hydrophysics*, 12(4), pp. 49-58. https://doi.org/10.7868/S2073667319040063 (in Russian).
4. Markova, N.V. and Bagaev, A.V., 2016. The Black Sea Deep Current Velocities Estimated from the Data of Argo Profiling Floats. *Physical Oceanography*, (3), pp. 23-35. https://doi.org/10.22449/1573-160X-2016-3-23-35
5. Klyuvitkin, A.A., Ostrovskii, A.G., Lisitzin, A.P. and Konovalov, S.K., 2019. The Energy Spectrum of the Current Velocity in the Deep Part of the Black Sea. *Doklady Earth Sciences*, 488(2), pp. 1222-1226. https://doi.org/10.1134/S1028334X1910012X
6. Demyshev, S.G., Ivanov, V.A., Markova, N.V. and Cherkesov, L.V., 2007. Simulation of the Current Field in the Black Sea Based on Eddy-Resolving Model with Assimilation of Climatic Temperature and Salinity Fields. *Ecological Safety of Coastal and Shelf Zones and Comprehensive Use of Shelf Resources*, 15, pp. 215-226 (in Russian).
7. Zalesny, V.B., Diansky, N.A., Fomin, V.V., Moshonkin S.N. and Demyshev, S.G., 2012. Numerical Model of the Circulation of the Black Sea and the Sea of Azov. *Russian Journal of*

Numerical Analysis and Mathematical Modelling, 27(1), pp. 95-111. https://doi.org/10.1515/rnam-2012-0006

8. Zalesny, V.B., Gusev, F.V. and Moshonkin S.N., 2013. Numerical Model of the Hydrodynamics of the Black Sea and the Sea of Azov with Variational Initialization of Temperature and Salinity. *Izvestiya, Atmospheric and Oceanic Physics*, 49(6), pp. 642-658. https://doi.org/10.1134/S0001433813060133
9. Korotenko, K.A., 2015. Modeling Mesoscale Circulation of the Black Sea. *Oceanology*, 55(6), pp. 820-826. https://doi.org/10.1134/S0001437015060077
10. Dorofeev, V.L. and Sukhikh, L.I., 2016. Analysis of Variability of the Black Sea Hydrophysical Fields in 1993–2012 Based on the Reanalysis Results. *Physical Oceanography*, (1), pp. 33-47. https://doi.org/10.22449/1573-160X-2016-1-33-47
11. Korshenko, E.A., Diansky, N.A. and Fomin, V.V., 2019. Reconstruction of the Black Sea Deep-Water Circulation Using INMOM and Comparison of the Results with the ARGO Buoys Data. *Physical Oceanography*, 26(3), pp. 202-213. https://doi.org/10.22449/1573-160X-2019-3-202-213
12. Staneva, J.V., Dietrich, D.E., Stanev, E.V. and Bowman, M.J., 2001. Rim Current and Coastal Eddy Mechanisms in an Eddy-Resolving General Circulation Model. *Journal of Marine Systems*, 31(1-3), pp. 137-157. https://doi.org/10.1016/S0924-7963(01)00050-1
13. Gunduz, M., Özsoy, E. and Hordoir, R., 2020. A Model of Black Sea Circulation with Strait Exchange (2008–2018). *Geoscientific Model Development*, 13(1), pp. 121-138. https://doi.org/10.5194/gmd-13-121-2020
14. Demyshev, S.G., Dymova, O.A., Markova, N.V. and Piotukh, V.B., 2016. Numerical Experiments on Modeling of the Black Sea Deep Currents. *Physical Oceanography*, (2), pp. 34-45. https://doi.org/10.22449/1573-160X-2016-2-34-45
15. Dymova, O.A., Miklashevskaya, N.A. and Markova, N.V., 2019. Particularies of the Black Sea Deep-Water Circulation in Summer 2013. *Ecological Safety of Coastal and Shelf Zones of Sea*, (1), pp. 40-47. https://doi.org/10.22449/2413-5577-2019-1-40-47 (in Russian).
16. Markova, N.V. and Dymova, O.A., 2023. Conditions of Deep-Water Undercurrent Generation in the North-Eastern Black Sea. *Fluid Dynamics*, 58(5), pp. 852-863. https://doi.org/10.1134/S0015462823600591
17. Pavlushin, A.A., Shapiro, N.B., Mikhailova, E.N., and Korotaev, G.K., 2015. Two-layer Eddy-Resolving Model of Wind Currents in the Black Sea. *Physical Oceanography*, (5), pp. 3-21. https://doi.org/10.22449/1573-160X-2015-5-3-21
18. Pavlushin, A.A., Shapiro, N.B. and Mikhailova, E.N., 2017. The Role of the Bottom Relief and the β-effect in the Black Sea Dynamics. *Physical Oceanography*, (6), pp. 24-35. https://doi.org/10.22449/1573-160X-2017-6-24-35
19. Mikhailova, E.N. and Shapiro, N.B., 2014. Three-Dimensional Non-Hydrostatic Model of Submarine Discharge in the Sea Coastal Zone. *Morskoy Gidrofizicheskiy Zhurnal*, (4), pp. 28-50 (in Russian).
20. Efimov, V.V. and Yurovsky, A.V., 2017. Formation of Vorticity of the Wind Speed Field in the Atmosphere over the Black Sea. *Physical Oceanography*, (6), pp. 3-11. https://doi.org/10.22449/1573-160X-2017-6-3-11
21. Pavlushin, A.A., Shapiro, N.B. and Mikhailova, E.N., 2018. Influence of Seasonal Variability of the Wind Stress Vorticity on the Structure of the Black Sea Circulation. *Physical Oceanography*, 25(5), pp. 345-358. https://doi.org/10.22449/1573-160X-2018-5-345-358
22. Zatsepin, A.G., Kremenetskiy, V.V., Stanichny, S.V. and Burdyugov, V.M., 2010. Black Sea Basin-Scale Circulation and Mesoscale Dynamics under Wind Forcing. In: A. V. Frolov and Yu. D. Resnyansky, eds., 2010. *Modern Problems of Ocean and Atmosphere Dynamics. The Pavel S. Lineykin Memorial Volume*. Moscow: TRIADA LTD, pp. 347-368 (in Russian).

23. Belonenko, T.V., Foux, V.R. and Zakharchuk, E.A., 2010. *Gradient-Vorticity Waves in the World Ocean*. LAP Lambert Academic Publishing GmbH & Co. KG, 408 p.

24. Zhmur, V.V., Novoselova, E.V. and Belonenko, T.V., 2021. Potential Vorticity in the Ocean: Ertel and Rossby Approaches with Estimates for the Lofoten Vortex. *Izvestiya, Atmospheric and Oceanic Physics*, 57(6), pp. 632-641. https://doi.org/10.1134/S0001433821050157

25. Pavlushin, A.A., 2022. Self-Oscillations of Large-Scale Circulation Intensity in the Black Sea. *Physical Oceanography*, 29(6), pp. 587-601. https://doi.org/10.22449/1573-160X-2022-6-587-601

26. Zatsepin, A.G., Elkin, D.N., Korzh, A.O., Kuklev, S.B., Podymov, O.I., Ostrovskii, A.G. and Soloviev, D.M., 2016. On Influence of Current Variability in the Deep Black Sea upon Water Dynamics of Narrow North Caucasian Continental Shelf. *Physical Oceanography*, (3), pp. 14-22. doi:10.22449/1573-160X-2016-3-14-22

Submitted 23.12.2024; approved after review 23.01.2025;
accepted for publication 15.05.2025.

About the author:

Andrey A. Pavlushin, Junior Research Associate, Marine Hydrophysical Institute of RAS (2 Kapitanskaya Str., Sevastopol, 299011, Russian Federation), **ORCID ID: 0000-0002-2098-5068**, **Scopus Author ID: 57142406500**, **ResearcherID: R-4908-2018**, **SPIN-code: 1439-2290**, pavlushin@mhi-ras.ru

The author has read and approved the final manuscript.
The author declares that he has no conflict of interest.